THE PRIMORDIAL DEUTERIUM ABUNDANCE OF THE MOST METAL-POOR DAMPED Lyα SYSTEM[*]

RYAN J. COOKE[1,2,8], MAX PETTINI[3,4], KENNETH M. NOLLETT[5], AND REGINA JORGENSON[6,7]
[1] UCO/Lick Observatory, University of California Santa Cruz, Santa Cruz, CA 95064, USA; rcooke@ucolick.org
[2] Kavli Institute for Particle Astrophysics and Cosmology (KIPAC), Stanford University, 452 Lomita Mall, Stanford, CA 94305, USA
[3] Institute of Astronomy, Madingley Road, Cambridge CB3 0HA, UK
[4] Kavli Institute for Cosmology, Madingley Road, Cambridge CB3 0HA, UK
[5] Department of Physics, San Diego State University, 5500 Campanile Drive, San Diego, CA 92182, USA
[6] Physics Department, Willamette University, 900 State Street, Salem, OR 97301, USA
[7] Maria Mitchell Observatory, 4 Vestal Street, Nantucket, MA 02554, USA
Received 2016 January 1; revised 2016 May 6; accepted 2016 May 23; published 2016 October 18

ABSTRACT

We report the discovery and analysis of the most metal-poor damped Lyα (DLA) system currently known, which also displays the Lyman series absorption lines of neutral deuterium. The average [O/H] abundance of this system is [O/H] = -2.804 ± 0.015, which includes an absorption component with [O/H] = -3.07 ± 0.03. Despite the unfortunate blending of many weak D I absorption lines, we report a precise measurement of the deuterium abundance of this system. Using the six highest-quality and self-consistently analyzed measures of D/H in DLAs, we report tentative evidence for a subtle decrease of D/H with increasing metallicity. This trend must be confirmed with future high-precision D/H measurements spanning a range of metallicity. A weighted mean of these six independent measures provides our best estimate of the primordial abundance of deuterium, $10^5\,(D/H)_P$ = 2.547 ± 0.033 ($\log_{10}(D/H)_P = -4.5940 \pm 0.0056$). We perform a series of detailed Monte Carlo calculations of Big Bang nucleosynthesis (BBN) that incorporate the latest determinations of several key nuclear reaction cross-sections, and propagate their associated uncertainty. Combining our measurement of $(D/H)_P$ with these BBN calculations yields an estimate of the cosmic baryon density, $100\,\Omega_{B,0}\,h^2(BBN) = 2.156 \pm 0.020$, if we adopt the most recent theoretical determination of the $d\,(p,\,\gamma)^3$He reaction rate. This measure of $\Omega_{B,0}\,h^2$ differs by $\sim 2.3\sigma$ from the Standard Model value estimated from the *Planck* observations of the cosmic microwave background. Using instead a $d\,(p,\,\gamma)^3$He reaction rate that is based on the best available experimental cross-section data, we estimate $100\,\Omega_{B,0}\,h^2(BBN) = 2.260 \pm 0.034$, which is in somewhat better agreement with the *Planck* value. Forthcoming measurements of the crucial $d\,(p,\,\gamma)^3$He cross-section may shed further light on this discrepancy.

Key words: cosmology: observations – cosmology: theory – primordial nucleosynthesis – quasars: absorption lines – quasars: individual (J1358+0349)

1. INTRODUCTION

Moments after the Big Bang, a brief period of nucleosynthesis created the first elements and their isotopes (Hoyle & Tayler 1964; Peebles 1966; Wagoner et al. 1967), including hydrogen (H), deuterium (D), helium-3 (^{3}He), helium-4 (^{4}He), and a small amount of lithium-7 (^{7}Li). The creation of these elements, commonly referred to as Big Bang nucleosynthesis (BBN), was concluded in $\lesssim 15$ minutes and currently offers our earliest reliable probe of cosmology and particle physics (for a review, see Steigman 2007, 2012; Iocco et al. 2009; Cyburt et al. 2016).

The amount of each primordial nuclide that was made during BBN depends most sensitively on the expansion rate of the universe and the number density ratio of baryons-to-photons. Assuming the Standard Model of cosmology and particle physics, the expansion rate of the universe during BBN is driven by photons, electrons, positrons, and three neutrino families. Furthermore, within the framework of the Standard Model, the baryon-to-photon ratio at the time of BBN (i.e., minutes after the Big Bang) is identical to the baryon-to-photon

ratio at recombination ($\sim$400,000 years after the Big Bang). Thus, the abundances of the primordial nuclides for the Standard Model can be estimated from observations of the Cosmic Microwave Background (CMB) radiation, which was recently recorded with exquisite precision by the *Planck* satellite (Planck Collaboration et al. 2016). Using the *Planck* CMB observations,[9] the predicted Standard Model abundances of the primordial elements are (68% confidence limits; see Section 5)

$$Y_P = 0.2471 \pm 0.0005,$$
$$10^5\,(D/H)_P = 2.414 \pm 0.047,$$
$$10^5\,(^3He/H)_P = 1.110 \pm 0.022,$$
$$A(^7Li/H)_P = 2.745 \pm 0.021,$$

where Y_P is the fraction of baryons consisting of ^{4}He, $A(^7Li/H)_P \equiv \log_{10}(^7Li/H)_P + 12$, and D/H, ^{3}He/H, and ^{7}Li/H are the number abundance ratios of deuterium, helium-3, and lithium-7 relative to hydrogen, respectively.

To test the Standard Model, the above predictions are usually compared to direct observational measurements of these abundances in near-primordial environments. High-precision measures of the primordial ^{4}He mass fraction are obtained from

---

[9] The primordial abundances listed here use the TT+lowP+lensing measure of the baryon density, $100\,\Omega_{B,0}\,h^2(CMB) = 2.226 \pm 0.023$, (i.e., the second data column of Table 4 from Planck Collaboration et al. 2016).

low-metallicity H II regions in nearby star-forming galaxies. Two analyses of the latest measurements, including an infrared transition that was not previously used, find $Y_P = 0.2551 \pm 0.0022$ (Izotov et al. 2014) and $Y_P = 0.2449 \pm 0.0040$ (Aver et al. 2015). These are mutually inconsistent, presumably due to some underlying difference between the analysis methods. The primordial ^{7}Li/H ratio is deduced from the most metal-poor stars in the halo of the Milky Way. The latest determination (Asplund et al. 2006; Aoki et al. 2009; Meléndez et al. 2010; Sbordone et al. 2010; Spite et al. 2015), $A(^7\text{Li}) = 2.199 \pm 0.086$, implies a $\gtrsim 6\sigma$ deviation from the Standard Model value (see Fields 2011 for a review). The source of this discrepancy is currently unknown. The abundance of ^{3}He has only been measured in Milky Way H II regions (Bania et al. 2002) and in solar system meteorite samples (Busemann et al. 2000, 2001). At this time, it is unclear if these measures are representative of the primordial value. However, there is a possibility that ^{3}He might be detected in emission from nearby, quiescent metal-poor H II regions with future, planned telescope facilities (Cooke 2015).

The primordial abundance of deuterium, $(\text{D/H})_P$, can be estimated using quasar absorption line systems (Adams 1976), which are clouds of gas that absorb the light from an unrelated background quasar. In rare, quiescent clouds of gas, the $-82\ \text{km s}^{-1}$ isotope shift of D relative to H can be resolved, allowing a measurement of the column density ratio D I/H I. The most reliable measures of $(\text{D/H})_P$ come from near-pristine damped Lyα systems (DLAs). As discussed in Pettini & Cooke (2012a) and Cooke et al. (2014), metal-poor DLAs exhibit the following properties that facilitate a high-precision and reliable determination of the primordial deuterium abundance. (1) The Lorentzian damped Lyα absorption line uniquely determines the total column density of neutral H atoms along the line of sight. (2) The array of weak, high-order D I absorption lines depends only on the total column density of neutral D atoms along the line of sight. Provided that these absorption lines fall on the linear regime of the curve of growth, the derived $N(\text{D I})$ should not depend on the gas kinematics or the instrument resolution. In addition, the assumption that $\text{D/H} = \text{D I/H I}$ is justified in these systems; the ionization correction is expected to be $\lesssim 0.1\%$ (Savin 2002; Cooke & Pettini 2016). Furthermore, galactic chemical evolution models suggest that most of the deuterium atoms in these almost pristine systems are yet to be cycled through many generations of stars; the correction for astration (i.e., the processing of gas through stars) is therefore negligible (see the comprehensive list of references provided by Cyburt et al. 2016; Dvorkin et al. 2016).

Using a sample of five quasar absorption line systems that satisfy a set of strict criteria, Cooke et al. (2014) recently estimated that the primordial abundance of deuterium is $\log_{10}(\text{D/H})_P = -4.597 \pm 0.006$ or, expressed as a linear quantity, $10^5 (\text{D/H})_P = 2.53 \pm 0.04$. These five systems exhibit a D/H plateau over at least a factor of ~ 10 in metallicity, and this plateau was found to be in good agreement with the expected value for the cosmological model supported by *Planck* assuming the Standard Model of particle physics. In this paper, we build on this work and present a new determination of the primordial abundance of deuterium obtained from the lowest-metallicity DLA currently known. In Section 2, we present the details of our observations and data reduction procedures. Our data analysis is almost identical to that described in Cooke et al. (2014), and we provide a

summary of this procedure in Section 3. In Section 4, we report the chemical composition of this near-pristine DLA. In Section 5, we present new calculations of BBN that incorporate the latest nuclear cross-sections, discuss the main results of our analysis, and highlight the cosmological implications of our findings. We summarize our conclusions in Section 6.

2. OBSERVATIONS AND DATA REDUCTION

In this paper, we present high-quality echelle observations of the quasar J1358+0349 ($z_{em} \simeq 2.894$, R.A. = $13^h58^m03^s.97$, decl. = $+03°49'36''.0$), which was discovered with a low-resolution ($R \sim 2000$) spectrum acquired by the Sloan Digital Sky Survey (SDSS). This SDSS spectrum revealed strong H I absorption at a redshift of $z_{abs} = 2.8528$ with no apparent absorption at the wavelengths of the corresponding metal lines, indicating the presence of a very metal-poor DLA. Penprase et al. (2010) reobserved this quasar with the Echellette Spectrograph and Imager (ESI), which is mounted on the Keck II telescope. These medium-resolution observations ($R \sim 5300$, corresponding to a velocity full width at half maximum $v_{\text{FWHM}} \simeq 57\ \text{km s}^{-1}$) confirmed that this DLA is among the most metal-poor systems currently known, with an estimated metallicity[10] of $[\text{Fe/H}] = -3.03 \pm 0.11$. We confirm the low metallicity with the higher-resolution data presented here; we find $[\text{Fe/H}] = -3.25 \pm 0.11$ (see Section 4), assuming a solar abundance $\log_{10}(\text{Fe/H})_\odot = -4.53$ (Asplund et al. 2009).

Identifying DLAs where the D I Lyman series absorption lines are well resolved from the much stronger H I Lyman series is one of the primary difficulties of finding DLAs where D/H can be measured. The probability of resolving these features can be increased by finding gas clouds with simple kinematics, which are more common at the lowest metallicity (Ledoux et al. 2006; Murphy et al. 2007; Prochaska et al. 2008; Jorgenson et al. 2013; Neeleman et al. 2013; Cooke et al. 2015); in general, the most metal-poor systems exhibit simple and quiescent kinematics. Given the low metallicity of the DLA toward J1358+0349, based on the ESI spectra, we acquired two high-quality, high-resolution spectra of this quasar with the aim of measuring D/H. We describe these observations below.

2.1. HIRES Observations

We observed J1358+0349 with the High Resolution Echelle Spectrometer (HIRES) (Vogt et al. 1994) on the Keck I telescope on 2013 May 6 in good seeing conditions ($\sim 0''.7$ FWHM) for a total of 21,000 s divided equally into 7×3000 s exposures. We used the blue-sensitive ultraviolet cross-disperser to maximize the efficiency near the DLA Lyman limit. We used the C1 decker ($7''.0 \times 0''.861$), which provides a nominal instrument resolution of $R \simeq 48,000$ ($v_{\text{FWHM}} \simeq 6.4\ \text{km s}^{-1}$) for a uniformly illuminated slit. By measuring the widths of 670 ThAr wavelength calibration lines,[11] we determined the instrument resolution to be

---

[10] Throughout this paper, we adopt the notation [X/Y] to represent the relative number density of elements X and Y on a logarithmic and solar abundance scale. Explicitly, $[\text{X/Y}] = \log_{10}(N(\text{X})/N(\text{Y})) - \log_{10}(n(\text{X})/n(\text{Y}))_\odot$.

[11] Ideally, O_2 telluric absorption should be used to determine the instrument resolution, since the broadening of these lines should closely represent the instrument resolution of the quasar absorption spectrum; unlike the sky and ThAr lamp emission lines, the quasar light does not uniformly illuminate the slit. However, the telluric O_2 molecular absorption band near 6300 Å was too weak to reliably measure the instrument FWHM.

$v_{\rm FWHM} = 6.17 \pm 0.02 \; \rm km \, s^{-1}$, which is somewhat lower than the nominal value. All frames were binned 2×2 during read-out. The science exposures were bracketed by a ThAr wavelength calibration frame. The final data cover the wavelength range 3480–6344 Å, with small gaps in the ranges 4397–4418 Å and 5397–5423 Å due to the gaps between the three HIRES detectors.

2.2. UVES Observations

The HIRES data confirmed the very low metallicity of the DLA and revealed several resolved D I absorption lines, suggesting that this system would be ideal to estimate the primordial deuterium abundance. To increase the signal-to-noise ratio (S/N) of the data, we observed J1358+0349 for a total of 40,384 s with the Very Large Telescope (VLT) Ultraviolet and Visual Echelle Spectrograph (UVES; Dekker et al. 2000) in service mode.[12] We used dichroic 1, with the HER_5 filter in the blue arm and the SHP700 filter in the red arm. The echelle grating in the blue arm provided a central wavelength of 3900 Å, while the grating in the red arm had a central wavelength of 5640 Å. The UVES data cover the wavelength range 3450–6648 Å, with small gaps in the ranges 4530–4622 Å and 5601–5675 Å. All exposures were binned 2×2 at the time of read-out. We used the 0″9 slit to match closely the nominal resolution provided by the HIRES observations (the nominal UVES values are $R \simeq 46{,}000$, $v_{\rm FWHM} \simeq 6.5 \; \rm km \, s^{-1}$). By fitting 268 ThAr emission lines, we derived an instrumental resolution of $v_{\rm FWHM} = 6.39 \pm 0.04 \; \rm km \, s^{-1}$ for a uniformly illuminated slit with our setup. Our value is in good agreement with the nominal UVES instrument resolution.[13]

2.3. Data Reduction

The HIRES and UVES data described above provide complete wavelength coverage from the DLA Lyman limit (~3520 Å) to 6648 Å (1725 Å in the rest frame of the DLA). The data were reduced with the HIRESRedux and UVESRedux[14] software packages, maintained by J. X. Prochaska (for a description of the reduction algorithms, see Bernstein et al. 2015). The standard reduction steps were followed. First, the bias level was subtracted from all frames using the overscan region. The pixel-to-pixel variations were then removed using an archived image where the detector was uniformly illuminated. The orders were defined using a quartz lamp with an identical slit and setup as the science exposures. A ThAr lamp was used to model the regions of constant wavelength across the detector (e.g., Kelson 2003). Using this model, the sky background was subtracted from the science exposure. The spectrum of the quasar was extracted using an optimal extraction algorithm, and mapped to a vacuum, heliocentric wavelength scale with reference to the ThAr exposure.

Each echelle order was corrected for the echelle blaze function, resampled onto a 2.5 km s^{-1} pixel scale, and

combined using the UVES_POPLER software.[15] Since the HIRES and UVES data were acquired with slightly different instrument resolutions, we separately combined the UVES and HIRES data. Deviant pixels and ghosts were manually removed, and an initial estimate of the quasar continuum was applied. The data were flux calibrated using the SDSS discovery spectrum as a reference. Specifically, the UVES and HIRES data were convolved with the SDSS instrument resolution, and then resampled onto the wavelength scale of the SDSS spectrum to determine the sensitivity function. The sensitivity function was then applied to the non-convolved UVES and HIRES data, with an extrapolation to blue wavelengths where the SDSS spectrum does not extend. The final HIRES spectrum has a S/N near the DLA Lyα absorption line of S/N $\simeq$ 30, and a S/N $\simeq$ 16 near the Lyman limit of the DLA. The equivalent values for UVES are S/N $\simeq$ 40 and S/N $\simeq$ 11, respectively.

3. ANALYSIS METHOD

Our analysis method is identical to that outlined by Cooke et al. (2014). In this section, we summarize the main aspects of this procedure. We use the Absorption LIne Software (ALIS) package to provide a simultaneous fit to the emission spectrum of the quasar and the absorption lines of the DLA.[16] ALIS uses a chi-squared minimization procedure to deduce the model parameter values that best fit the data, weighted by the quasar error spectrum.

Our line fitting procedure was applied at the same time to both the UVES and HIRES data, to find the model that fitted *both* sets of data best. We simultaneously fit the H I and D I Lyman series absorption lines, all of the significantly detected metal absorption lines, the zero-levels of the HIRES and UVES data, the continuum in the neighborhood of all absorption lines, the relative velocity offset between the HIRES and UVES data, and the instrument resolution of both data sets. The continuum is approximated by a low-order Legendre polynomial (typically of order $\lesssim 4$, except near Lyα where we use a polynomial of order 8). To allow for relative differences in the quasar continuum between the HIRES and UVES data, we apply a constant or linear scaling to the HIRES data, and the parameters of this scaling are allowed to vary during the minimization procedure.

The portion of the Lyα absorption profile where the optical depth is $\tau \gtrsim 1$ provides most of the power to determine the total H I column density; when the quasar flux recovers to $\gtrsim 50\%$ of the continuum, the absorption profile flattens and becomes increasingly sensitive to the continuum level rather than the H I absorption. We therefore fit every pixel in the core of the Lyα absorption until the Lorentzian wings of the profile are 50% of the continuum (i.e., $\tau \gtrsim 0.7$; in this case, all pixels within ± 1300 km s^{-1}). During the analysis, we fit all of the contaminating absorption features within this velocity window instead of masking the affected pixels. Outside this velocity window, we include pixels in the fit that we deem are free of contamination. The best-fitting model of the Lyα absorption feature is overlaid on the HIRES and UVES data in Figure 1.

Our spectrum includes 16 metal absorption lines from the elements C, N, O, Al, Si, S, and Fe in a range of ionization

---

[12] Our observations were carried out on 2014 March 28 (3×3495 s), 2014 May 27 (3×3495 s), 2014 March 24 (4×3495 s), and 2014 April 30 (1×3495 s, 1×1939 s).

[13] We note that the telluric O_2 molecular absorption band near 6300 Å was too weak, like the HIRES data, to reliably measure the instrument FWHM.

[14] These reduction packages can be obtained from http://www.ucolick.org/~xavier/HIRedux/index.html.

[15] UVES_POPLER can be downloaded from http://astronomy.swin.edu.au/~mmurphy/UVES_popler/.

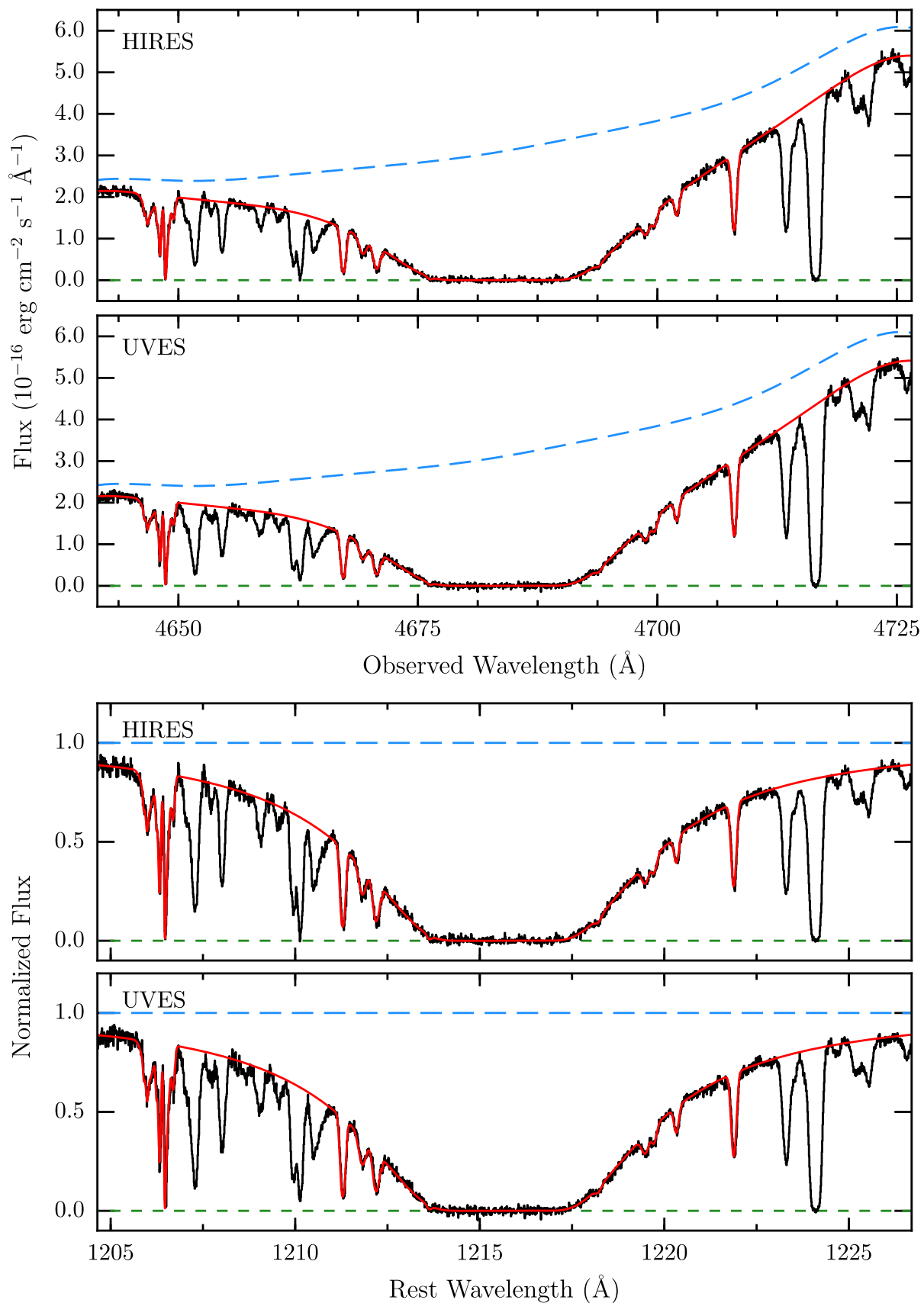[16] ALIS is available for download at the following website: https://github.com/rcooke-ast/ALIS.

Figure 1. Top panels: the flux calibrated H I Lyα absorption profile (black histogram) is shown for the DLA at $z_{abs} = 2.853054$ toward the quasar J1358+0349. The best-fitting quasar continuum model (blue long-dashed curves) and the best-fitting absorption profile (red line) are overlaid. The green dashed line indicates the fitted zero-level of the data. The spectrograph used to take the data is indicated in the upper left corner of each panel. Bottom panels: same as the top panels, but with the quasar continuum normalized, and the data are plotted in the rest frame of the DLA. The absorption feature that is fit near a rest wavelength of 1206.5 is a combination of the Si III absorption from the DLA and an unrelated blend.

Table 1
Best-fitting Model Parameters for the DLA at $z_{abs} = 2.853054$ toward the QSO J1358+0349

Comp.	z_{abs}	b_{turb} $(km\,s^{-1})$	$\log N(\text{H\,I})$ (cm^{-2})	$\log(\text{D\,I/H\,I})$	$\log N(\text{N\,I})$ (cm^{-2})	$\log N(\text{N\,II})$ (cm^{-2})	$\log N(\text{N\,III})$ (cm^{-2})
1	2.852874	4.7	20.16	−4.582[a]	12.61	…[b]	…[b]
	±0.000002	±0.2	±0.02	±0.012	±0.10		
2	2.853004	3.9	…[b]	…[b]	…[b]	13.25[c]	13.32[c]
	±0.000003	±0.3				±0.04	±0.06
3	2.853054	2.5	20.27	−4.582[a]	12.23	…[b]	13.33
	±0.000003	±0.5	±0.02	±0.012	±0.24		±0.06
4	2.85372	14.2	18.23	−4.582[a]	…[b]	…[b]	12.60
	±0.00001	±1.4	±0.07	±0.012			±0.13
Total	…	…	20.524	−4.582[a]	12.77	13.25	13.67
			±0.006	±0.012	±0.11	±0.04	±0.02

Comp.	$\log N(\text{O\,I})$ (cm^{-2})	$\log N(\text{Al\,II})$ (cm^{-2})	$\log N(\text{Si\,II})$ (cm^{-2})	$\log N(\text{Si\,III})$ (cm^{-2})	$\log N(\text{S\,II})$ (cm^{-2})	$\log N(\text{Fe\,II})$ (cm^{-2})
1	14.23	11.27	12.78	…[b]	…[b]	12.31
	±0.02	±0.07	±0.03			±0.18
2	…[b]	11.93	12.94	12.89	13.02	12.51
		±0.02	±0.04	±0.12	±0.10	±0.11
3	13.89	…[b]	12.57	12.65	…[b]	…[b]
	±0.02		±0.08	±0.10		
4	12.86	…[b]	…[b]	12.19	…[b]	…[b]
	±0.12			±0.04		
Total	14.41	12.01	13.27	13.14	13.02	12.74
	±0.01	±0.02	±0.01	±0.07	±0.10	±0.10

Notes.
[a] Forced to be the same for all components.
[b] Absorption is undetected for this ion in this component.
[c] Since the N II and N III absorption lines arise from more highly ionized gas, we tie their total Doppler parameter, and allow it to vary independently of the Doppler parameter of the other absorption lines at the redshift of this component. The total Doppler parameter for these higher stages of N ionization is $b = 10.5 \pm 0.9\ km\,s^{-1}$.

stages, (C II, C IV, N I, N II, N III, O I, Al II, Si II, Si III, Si IV, S II, and Fe II). The component structure of our absorption model (see Table 1) is set by the unblended, narrow metal absorption lines that are the dominant ionization stage in neutral gas. The metal absorption lines that are used in our analysis are presented in Figure 2. We find that the neutral N I and O I lines, which accurately trace the D I bearing gas (Cooke & Pettini 2016, see also, Field & Steigman 1971; Steigman et al. 1971), are reproduced with just two principal absorption components. The strong O I λ1302 absorption line also exhibits a much weaker absorption feature, comprising ~3% of the total O I column density, and is redshifted by $v \simeq +50\ km\,s^{-1}$ relative to the two main components; this feature is also detected in the strong C II λ1334 and Si II λ1260 absorption lines (not shown). The first and higher ions, such as N II, Al II, Si II, and S II, require an additional absorption component that is slightly blueshifted by $v \simeq -4\ km\,s^{-1}$ relative to the systemic redshift $z_{abs} = 2.853054$, and is presumably due to ionized gas.

We explicitly fit to the D I/H I ratio by requiring that all D I absorption components (i.e., components 1, 3, and 4 in Table 1) have the same D/H ratio. Note that the subdominant D I absorption component (component 4, located at $+50\ km\,s^{-1}$ relative to the systemic redshift of the DLA) is not resolved from the H I absorption; the absorption properties of this component are only determined by the H I and O I absorption. The initial starting value of the logarithmic D I/H I ratio was randomly generated on the interval $(-4.8, -4.4)$. We assume that the absorption lines of all species are represented by a Voigt profile, comprising contributions from both turbulent and

thermal broadening. The standard assumption is that all gas constituents in a given absorption component will share a common turbulent Doppler parameter and a constant kinetic temperature. As we discuss in Cooke et al. (2014), at the current level of precision, a Voigt profile that is broadened according to the above description is probably insufficient to accurately model the H I, D I, and metal absorption lines simultaneously; in reality, there is a distribution of turbulence and temperature along the line of sight. To circumvent this model limitation, we tie the component redshifts and turbulent Doppler parameters of all ions, and allow the thermal broadening to be specified separately for the D I and H I absorption. This prescription allows the kinematics of the H I, D I, and metal absorption lines to be deduced almost independently. We also stress that, as discussed in Cooke et al. (2014), weak unblended D I absorption lines do not depend on the form of the Voigt profile; the equivalent widths of weak D I absorption lines uniquely determine the D I column density. Similarly, the absorption profile of the H I damped Lyα absorption line is independent of the turbulence and kinetic temperature used for the Voigt profile fitting.

Our HIRES and UVES data of the Lyman series absorption lines, together with the best-fitting model, are presented in Figures 3 and 4. In our analysis, we only use the H I absorption lines that exhibit either a clean blue or clean red wing. Similarly, we only consider the D I absorption lines that are free of unrelated contaminating absorption. These include D I Ly6, Ly7, Ly9, and Ly13; of these, only Ly9 and Ly13 are weak, unsaturated absorption lines. We also note that D I Ly13 is barely resolved from the H I Ly14 absorption (see bottom
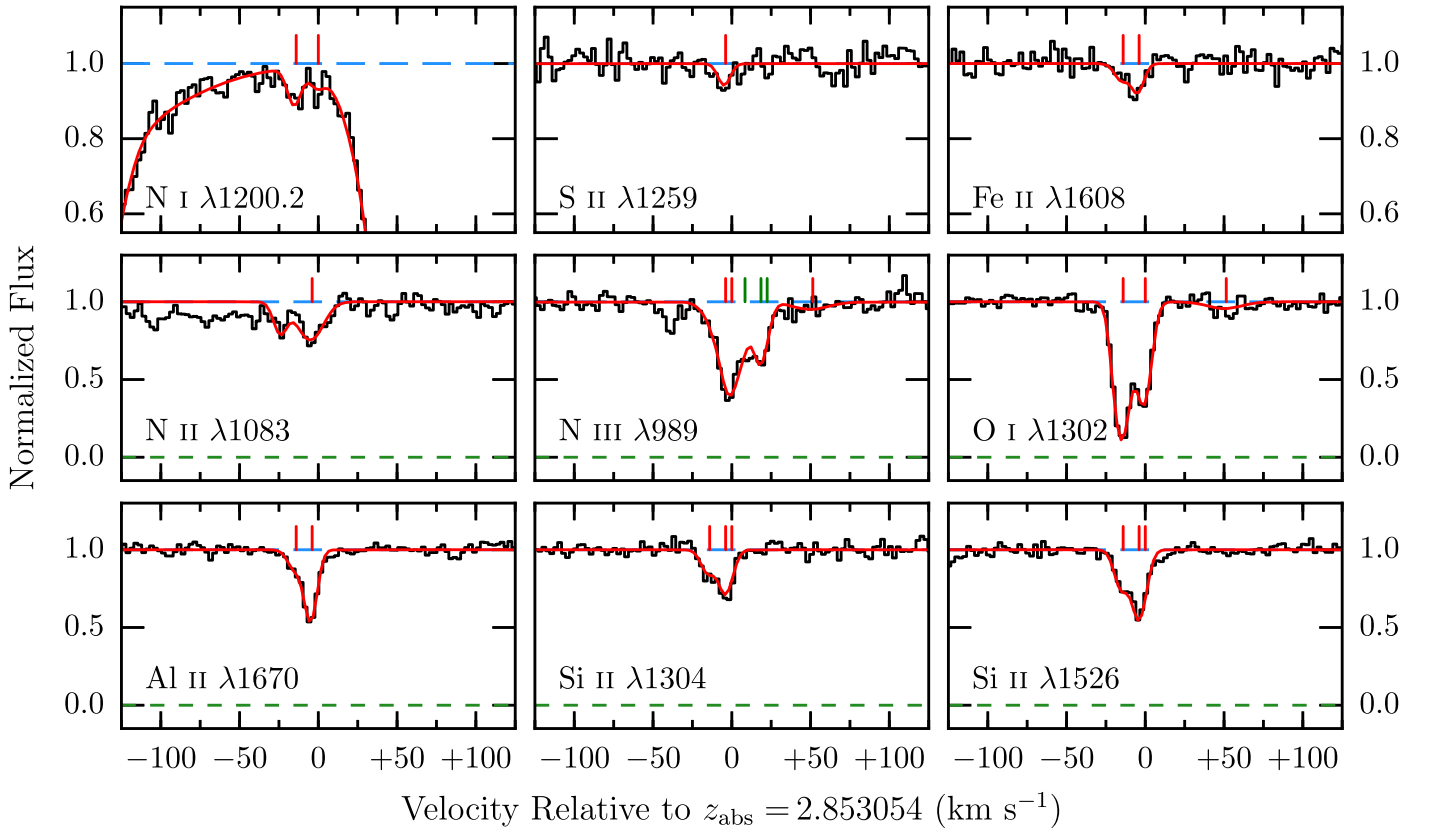
Figure 2. Selection of the metal absorption lines associated with the DLA at z_{abs} = 2.853054 toward J1358+0349 that are used in our analysis. The best-fitting model (red line) is derived from a simultaneous fit to both the UVES and HIRES data. However, in these panels we only show the data (black histogram) and corresponding model for the data set with the higher S/N near the absorption line. In all panels, the best-fitting zero-level of the data (short green dashed line) has been removed, and the continuum has been normalized (long blue dashed line). Note that we have used a different y-axis scale for the top row of panels to emphasize the weakest absorption features. The red tick marks above the spectrum correspond to the locations of the absorption components of the annotated ion (see Table 1). The green tick marks in the N III λ989 panel are for a blend with Si II λ989, the latter of which is largely determined from the multitude of other Si II absorption lines. The absorption at -25 km s^{-1} in the N II λ1083 panel is assumed to be an unrelated blend.

panels of Figure 4). Since the H I Ly14 absorption is well constrained by the host of other H I Lyman series lines, we deem the D I equivalent width of Ly13 (particularly from the HIRES data) to be well-determined. However, the DLA system that we analyze here is certainly less ideal for the determination of D/H than our previously reported cases in Pettini & Cooke (2012a) and Cooke et al. (2014). In this new system, many of the weak D I absorption lines are blended with unrelated absorption features (presumably contamination from low-redshift Lyα absorption),[17] resulting in fewer unsaturated D I lines. However, we are still able to constrain the value of the D/H ratio within tight limits, thanks to the high S/N of our data near the Lyman limit of the DLA, and the relatively well-determined value of the H I column density.

Initially, the instrumental FWHM was allowed to vary freely, with no prior (as implemented in Cooke et al. 2014). In this case, the fitted value of the instrumental FWHM was larger than that allowed by the widths of the ThAr arc lines (see Section 2), implying that the DLA absorption lines are too structured to permit a reliable estimate of the FWHM. Thereafter, we fixed the instrumental FWHM to be equal to the widths of the ThAr emission lines.

Finally, the relative velocity shift between the HIRES and UVES data is determined during the χ^2-minimization process, with a best-fitting value of 0.20 ± 0.12 km s^{-1}. We also fit a wavelength independent correction to the zero-level of each spectrum. This approximation also accounts for the fraction of the quasar light that is not covered by the DLA absorption. The best-fit values[18] for the zero-level are 0.016 ± 0.003 (HIRES) and 0.003 ± 0.003 (UVES).

Our analysis was performed blindly, such that the N(D I)/N(H I) ratio was only revealed after our profile analysis had been finalized, and the minimum χ^2 had been reached; no changes were made to the data reduction or analysis after the results were unblinded. We then performed 2000 Monte Carlo simulations to ensure that the global minimum χ^2 had been found. Each Monte Carlo simulation was initialized with the best-fitting model parameters, perturbed by twice the covariance matrix of the parameter values. The final parameter values listed in Table 1 correspond to the model with χ^2/dof = 7770/8678, that provides the global minimum chi-squared.[19]

---

[17] This is one of the unpredictable, and inherent difficulties associated with measuring the D/H ratio in $z \sim 3$ quasar absorption line systems.

[18] This parameter is largely driven by the trough of the Lyα absorption.

[19] As discussed in Cooke et al. (2014), the χ^2 value reported here should not be used for a statistical analysis, since (1) correlations between pixels are not accounted for, and (2) the selected wavelength regions used for fitting tend to be those with smaller statistical fluctuations.
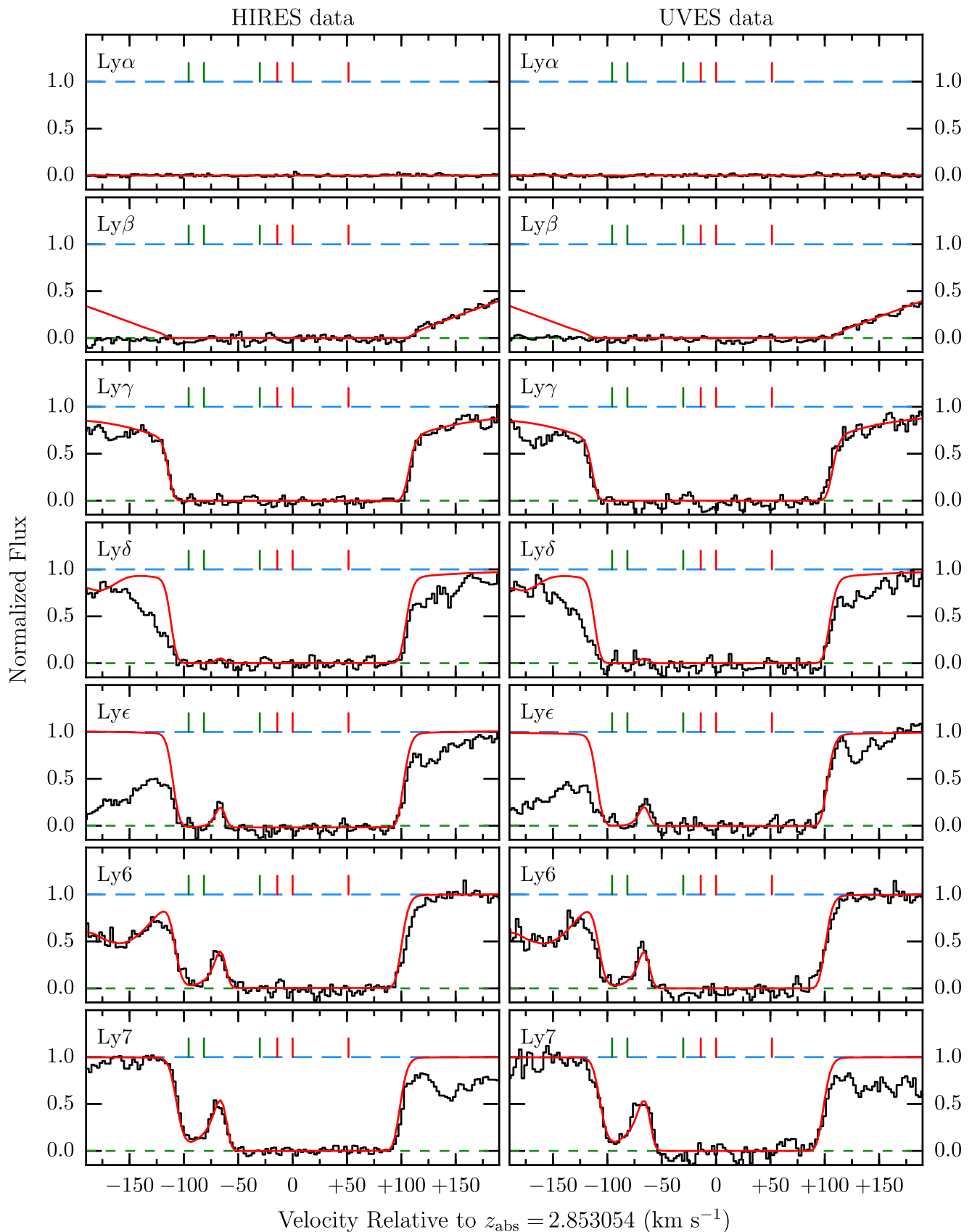
Figure 3. The black histogram shows our HIRES data (left panels) and UVES data (right panels), covering the H I and D I Lyman series absorption lines from Lyα–Ly7 (top to bottom panels, respectively). Our best-fitting model is overlaid with the solid red line. The plotted data have been corrected for the best-fitting zero-level (short green dashed line), and are normalized by the best-fitting continuum model (long blue dashed line). Tick marks above the spectrum indicate the absorption components for H I (red ticks) and D I (green ticks).
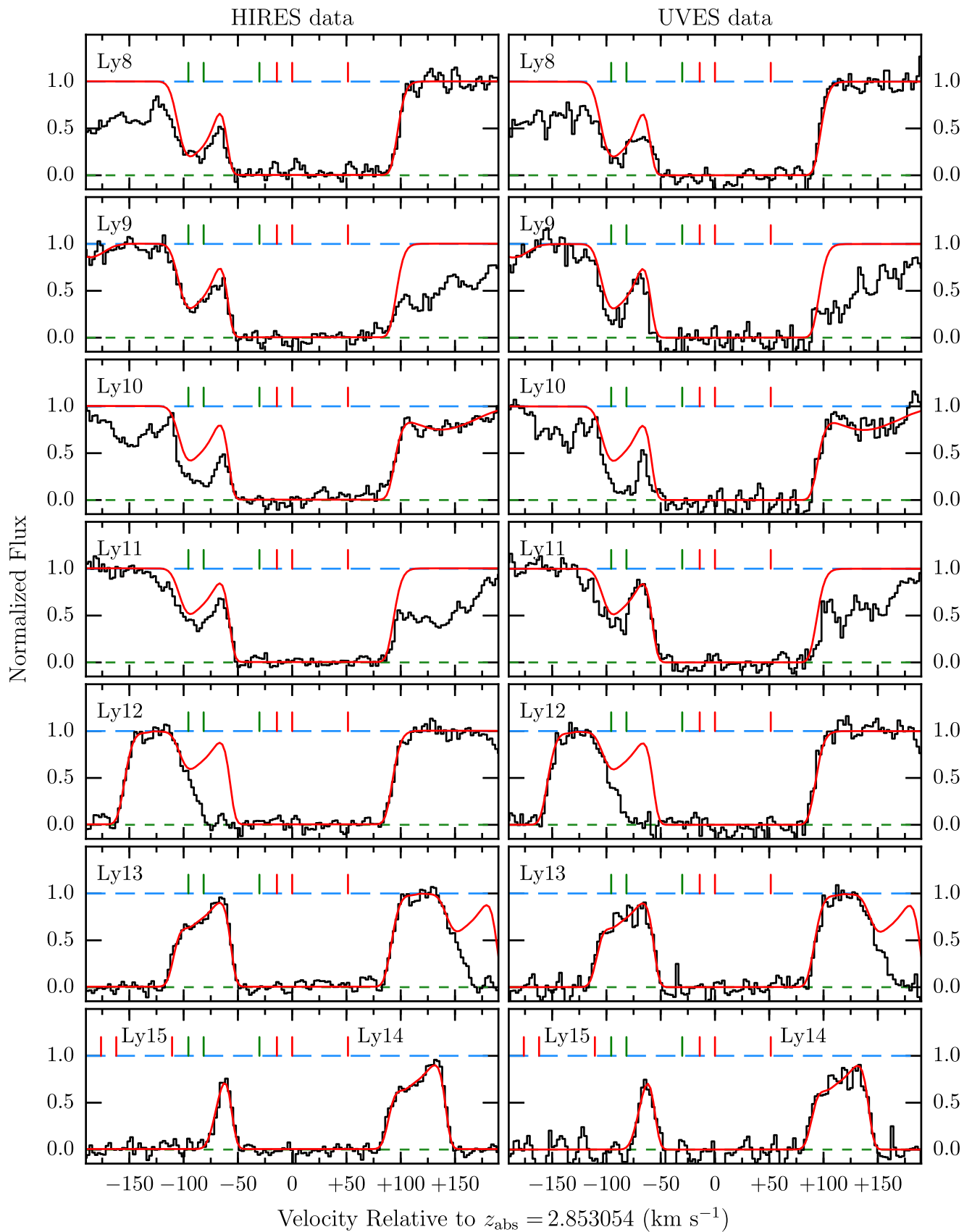
Figure 4. Same as Figure 3, for the H I and D I transitions Ly8–Ly15. Note that the leftmost set of red tick marks in the bottom panels indicate the H I Ly15 absorption components, while the central red tick marks in these panels indicate H I Ly14 absorption.

Table 2
Chemical Composition of the DLA at $z_{abs} = 2.853054$ toward J1358+0349

X	$\log \epsilon(X)_\odot$[a,b]	[X/H][c]	[X/O][c]	$[X/O]_1$[d]
N	7.83	-3.58 ± 0.11	-0.78 ± 0.11	-0.76 ± 0.10
O	8.69	-2.804 ± 0.015	...	...
Al	6.44	< -2.95	< -0.15	-0.71 ± 0.07
Si	7.51	< -2.764	$< +0.04$	-0.27 ± 0.04
S	7.14	< -2.64	$< +0.16$	...
Fe	7.47	< -3.25	< -0.45	-0.70 ± 0.18

Notes.
[a] $\log \epsilon(X) = 12 + \log N(X)/N(H)$.
[b] Asplund et al. (2009).
[c] Limits are quoted for the first ions due to the presence of ionized gas.
[d] The final column lists the element abundance ratios of the mostly neutral absorption component at $z_{abs} = 2.852874$ (i.e., component number 1).

4. DLA CHEMICAL COMPOSITION

The chemistry of the DLA at $z_{abs} = 2.853054$ toward the quasar J1358+0349 is remarkable for several reasons. On the basis of six O I lines, we determine the average metallicity of the DLA to be [O/H] $= -2.804 \pm 0.015$, assuming a solar O abundance of $\log (O/H)_\odot = -3.31$ (Asplund et al. 2009). This cloud is therefore the most pristine DLA currently known (see Cooke et al. 2011b). Furthermore, under our assumption that D I/H I is constant between the two main components, the O abundance of the strongest H I absorption (component 3 in Table 1) is [O/H] $= -3.07 \pm 0.03$.

We list the absolute and relative element abundances of this DLA in Table 2. Due to the presence of ionized gas (see Section 3), we quote upper limits on the abundances of Al, Si, S, and Fe; the first ions of these elements are the dominant stage of ionization in neutral (H I) gas, but are also present in ionized (H II) gas. We also note that the [N/O] ratio is well-determined in this DLA, since both N I and O I trace the H I bearing gas due to charge transfer reactions (Field & Steigman 1971; Steigman et al. 1971). Our value of [N/O] is consistent with, or slightly lower than, the primary N/O plateau (Izotov & Thuan 1999; Centurión et al. 2003; van Zee & Haynes 2006; Petitjean et al. 2008; Pettini et al. 2008; Pettini & Cooke 2012b; Zafar et al. 2014).

In the final column of Table 2, we also list the relative element abundances of component 1 ($z_{abs} = 2.852874$); this absorption component probably arises from predominantly neutral gas, since the higher stages of ionization are not detected in this component (see Table 1). Therefore, if the metals are well-mixed in this near-pristine DLA,[20] then component 1 should reflect the chemistry of this system. Relative to a typical metal-poor DLA (Cooke et al. 2011b), we find that this absorption component is somewhat enhanced in oxygen relative to Al, Si, and Fe. It is not unexpected that the lighter elements, such as C and O, exhibit an enhancement relative to the heavier elements (e.g., Fe) in the lowest-metallicity DLAs (Cooke et al. 2011a; Cooke & Madau 2014); this could be a signature of the (washed out?) chemical enrichment from the first generation of stars (e.g., Umeda & Nomoto 2003).

---

[20] Note that chemical variations have not been observed in other low-metallicity DLAs (Prochaska 2003; Cooke et al. 2011b).

5. THE DEUTERIUM ABUNDANCE

The near-pristine gas in the DLA reported here is a highly suitable environment for measuring the primordial abundance of deuterium (see also Fumagalli et al. 2011 for the most metal-poor Lyman Limit system). However, as discussed in Section 3, the structure of the absorption lines and the unfortunate level of unrelated contamination limit the *accuracy* with which the deuterium abundance can be measured in this system. The measured value of D I/H I in this DLA, expressed as a logarithmic and linear quantity, is

$$\log_{10} (D I/H I) = -4.582 \pm 0.012, \qquad (1)$$

$$10^5\, D I/H I = 2.62 \pm 0.07, \qquad (2)$$

which is consistent with the inverse variance weighted mean value of the five other high-precision measurements reported by Cooke et al. (2014), $10^5\, D I/H I = 2.53 \pm 0.04$. The D I/H I measurement precision obtained from this new DLA is comparable to the systems analyzed by Cooke et al. (2014), reflecting the high S/N of our data and the well-determined value of the total H I column density.

Despite the very low metallicity of this system, we also detect weak absorption from N I and N II, resulting in an ion ratio $\log(N II/N I) = 0.48 \pm 0.12$. As recently highlighted by Cooke & Pettini (2016), charge transfer ensures that this ion ratio is sensitive to the relative ionization of deuterium and hydrogen in DLAs, and can be used to assess if an ionization correction must be applied to the measured D I/H I ratio to recover the true D/H abundance. Using Equation (28) from Cooke & Pettini (2016), we estimate that the D/H ionization correction for this system is

$$IC(D/H) \equiv \log_{10}(D/H) - \log_{10} N(D I)/N(H I), \qquad (3)$$

$$IC(D/H) = (-4.9 \pm 1.0) \times 10^{-4}, \qquad (4)$$

which includes a 6% uncertainty in the ionization correction relation, as recommended by Cooke & Pettini (2016). Since this correction is a factor of ~25 below the precision of this single measurement, we do not apply this correction to our results.

5.1. Metallicity Evolution

In what follows, we only consider the six highest-quality, and self-consistently analyzed D/H abundance measurements; this sample includes the new measurement that we report herein and the sample of five measurements previously analyzed by Cooke et al. (2014). These measures are presented as a function of [O/H] metallicity in Figure 5 and are listed in Table 3. For other recent D/H measures and a more extensive list of literature measurements, see Riemer-Sørensen et al. (2015) and Balashev et al. (2016).

A visual inspection of Figure 5 may suggest that there is a mild evolution (decline) of D/H with metallicity, given that the value deduced here for the lowest-metallicity DLA is the highest of the six high-precision measures. However, we caution that the trend is not statistically significant, given the small size of the current sample. Specifically, assuming a linear evolution of the D/H abundance with metallicity, we find

$$\begin{aligned} \log_{10} (D/H) \\ = (-4.583 \pm 0.010) - (2.8 \pm 2.0) \times 10^3 (O/H), \end{aligned} \qquad (5)$$

where $(O/H) = 10^{[O/H]-3.31} \equiv N(O I)/N(H I)$. The p-value of a non-evolving D/H ratio (rather than a linear evolution with
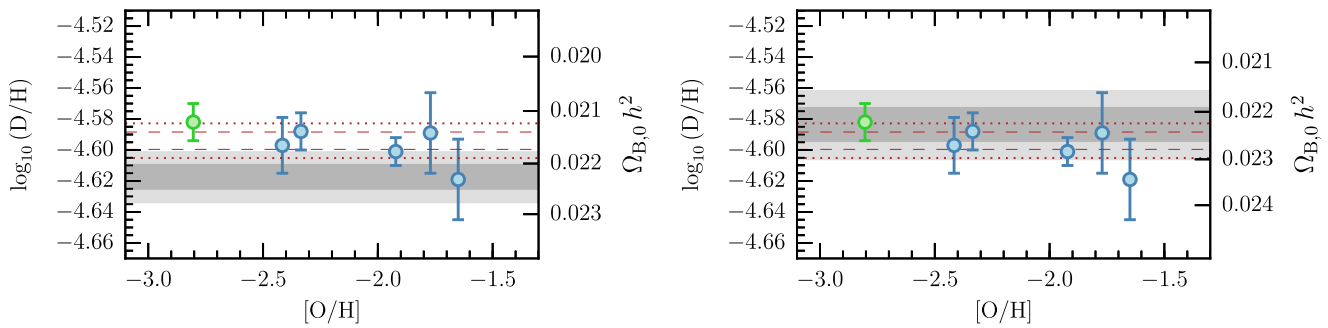
Figure 5. We plot the current sample of high-quality primordial D/H abundance measurements (symbols with error bars) as a function of the oxygen abundance. The green symbol (with the lowest value of [O/H]) corresponds to the new measurement reported here, and the blue symbols are taken from Cooke et al. (2014). The red dashed and dotted horizontal lines indicate the 68% and 95% confidence interval on the weighted mean value of the six high-precision D/H measures listed in Table 3. The right axes show the conversion between D/H and $\Omega_{B,0} h^2$ for the Standard Model. The conversion shown in the left panel uses the recent theoretical determination of the $d(p,\gamma){}^3$He reaction rate (and its error) by Marcucci et al. (2016a), while the right panel uses an empirical $d(p,\gamma){}^3$He rate and error based on the best available experimental data (see Nollett & Burles (2000) and Nollett & Holder (2011) for a critical assessment of the available experimental data). In both panels, the gray horizontal band shows the Standard Model D/H abundance based on our BBN calculations (see text) and the universal baryon density determined from the CMB temperature fluctuations (Planck Collaboration et al. 2016). The dark and light shades of gray represent the 68% and 95% confidence bounds, respectively, including the uncertainty in the conversion of $\Omega_{B,0} h^2$ to D/H (0.83% for the left panel and 2.0% for the right panel). The Standard Model value displayed in the left panel is 0.02 dex lower in $\log_{10}(D/H)$ than that shown in Figure 5 of Cooke et al. (2014). This shift is largely due to the updated *Planck* results (Planck Collaboration et al. 2016), and the updated theoretical $d(p,\gamma){}^3$He reaction rate (Marcucci et al. 2016a).

Table 3
Precision D/H Measures Considered in this Paper

QSO	$z_{\rm em}$	$z_{\rm abs}$	$\log N(H\ I)/{\rm cm}^{-2}$	[O/H][a]	$\log_{10}$ D I/H I
HS 0105+1619	2.652	2.53651	19.426 ± 0.006	-1.771 ± 0.021	-4.589 ± 0.026
Q0913+072	2.785	2.61829	20.312 ± 0.008	-2.416 ± 0.011	-4.597 ± 0.018
SDSS J1358+0349	2.894	2.85305	20.524 ± 0.006	-2.804 ± 0.015	-4.582 ± 0.012
SDSS J1358+6522	3.173	3.06726	20.495 ± 0.008	-2.335 ± 0.022	-4.588 ± 0.012
SDSS J1419+0829	3.030	3.04973	20.392 ± 0.003	-1.922 ± 0.010	-4.601 ± 0.009
SDSS J1558−0031	2.823	2.70242	20.75 ± 0.03	-1.650 ± 0.040	-4.619 ± 0.026

Note.
[a] We adopt the solar value log (O/H) + 12 = 8.69 (Asplund et al. 2009).

O/H) is 0.15, indicating that our null hypothesis (the D/H abundance is constant over the metallicity range of our sample) can only be rejected at the 1.4σ significance level.

It is intriguing that the tentative decline of D/H with increasing metallicity is in the same sense as expected from galactic chemical evolution. On the other hand, published models of the astration of D (see Cyburt et al. 2016 for a list of references) do not predict any significant evolution over the metallicity range relevant here. For example, the recent galactic chemical evolution models of Weinberg (2016) entertain very minor corrections for astration at the metallicities of the DLAs considered here (see also Romano et al. 2006; Dvorkin et al. 2016). Specifically, the D/H astration correction is estimated to be 0.33% and 0.023% (+0.0015 and +0.0001 in the log) from the least to the most metal-poor DLA listed in Table 3. These (systematic) upward corrections to D/H are significantly smaller than the random errors associated with the six measures of D/H.

For comparison, converting Equation (16) of Weinberg (2016) into the form of our Equation (5), we estimate a slope of ≈ -140 for their fiducial model, which is a factor of ~20 lower than the value estimated using the observational data, see Equation (5). This suggests that astration is not responsible for the mild evolution of D/H with metallicity (if there is one at all over the range of O/H values of our sample).

Another possibility is that deuterium may be preferentially depleted onto dust grains (Jura 1982; Draine 2004, 2006). This effect has been seen in the local interstellar medium of the Milky Way (Wood et al. 2004; Prochaska et al. 2005; Linsky

et al. 2006; Ellison et al. 2007; Lallement et al. 2008; Prodanović et al. 2010). However, unlike the Milky Way, the DLAs that we investigate here are very low metallicity ([Fe/H] < −2.0); even the most refractory elements in such DLAs exhibit negligible dust depletions (Pettini et al. 1997; Vladilo 2004; Akerman et al. 2005), and very low-metallicity DLAs are not expected to harbor a significant amount of dust (see Murphy & Bernet 2016, and references therein). Ultimately, this issue will be clarified by extending the number of precision measures of D/H over a wider range of metallicity than covered by the present sample.

5.2. Implications for Cosmology

As discussed above, the six self-consistently analyzed D/H abundance measurements that we consider here are statistically consistent with being drawn from the same value. Hereafter, we assume that all six measures provide a reliable estimate of the primordial abundance of deuterium, $(D/H)_P$. From the weighted mean of these independent values, we deduce our best estimate of the primordial deuterium abundance:

$$\log_{10}(D/H)_P = -4.5940 \pm 0.0056 \qquad (6)$$

or, expressed as a linear quantity:

$$10^5 (D/H)_P = 2.547 \pm 0.033. \qquad (7)$$

To compare our determination of $(D/H)_P$ with the latest *Planck* CMB results, we computed a series of detailed BBN calculations that include the latest nuclear physics input. Our

simulation suite is identical to that described by Nollett & Burles (2000), but includes updates to the following: (1) the neutron lifetime from Olive et al. (2014); (2) new experimental cross-section measurements for $d(d, n)^3$He, $d(d, p)^3$H (Greife et al. 1995; Leonard et al. 2006), and ^{3}He$(\alpha, \gamma)^7$Be (Cyburt et al. 2008; Adelberger et al. 2011); and (3) new theoretical cross-section calculations of $p(n, \gamma)d$ (Rupak 2000) and $d(p, \gamma)^3$He (Marcucci et al. 2016a). For further details on all but $d(p, \gamma)^3$He, see Nollett & Holder (2011).

The $d(p, \gamma)^3$He reaction rate can now be reliably computed with a precision of about 1%, compared with current laboratory measurements that have an uncertainty of $\gtrsim 7\%$. Our previous work used the $d(p, \gamma)^3$He reaction rate calculated by Marcucci et al. (2005). Recently, Marcucci et al. (2016a) have published a revised calculation, which includes a ~2.5% relativistic correction that had previously been found to be large in $d(n, \gamma)^3$H. The new calculation also includes a quantitative error estimate that is better than 1% at most energies and incorporates wave functions that have been extensively tested for accuracy. We use the numerical uncertainty quoted by Marcucci et al. (2016a) and do not use laboratory data to inform the theoretical rate (see, e.g., Coc et al. 2015); at BBN energies, the laboratory data predominantly consist of one experiment that has relatively low precision and is in moderate conflict with the calculation. For comparison, we also consider how the output nucleosynthesis is altered if we use the empirical $d(p, \gamma)^3$He reaction rate instead of the theoretical rate (see below). Although we use the numerical uncertainty quoted by Marcucci et al. (2016a), it should be pointed out that no quantitative estimate exists for further uncertainties in construction of the nucleon-nucleon potential and current operators, which could be of similar size. We have attempted to account for some of this with a 0.5% correlated error on all points of the curve.

We now describe a summary of our BBN calculations, and direct the reader to Nollett & Burles (2000) for further details. First, the calculations are initialized with a Gaussian random realization of each cross-section measurement or (in the cases of $p(n, \gamma)d$ and $d(p, \gamma)^3$He) calculation. The distributions of point-to-point errors and of the (usually larger) normalization errors shared by all points from a given experiment are sampled independently. Then a continuous, piecewise polynomial is fit to the sampled cross-sections. The thermal reaction rates at BBN temperatures are calculated for each realization, using the sampled and fitted cross-sections. These rates are used as input into a BBN code, along with a Gaussian random realization of the neutron lifetime, and the output nucleosynthesis is stored. At a given value of the expansion rate (parameterized by the number of neutrino species,[21] N_ν) and the density ratio of baryons-to-photons (η_{10}, in units of 10^{10}), we perform 24,000 Monte Carlo realizations, which was deemed to provide smooth 2σ confidence contours as a function of η_{10} (see Nollett & Burles 2000). This procedure provides a thorough accounting of the current error budget for primordial nucleosynthesis calculations.

We computed the resulting nucleosynthesis over the range $1.8 \leqslant N_\nu \leqslant 4$ (in steps of 0.2) and $0.477 \leqslant \log_{10} \eta_{10} \leqslant 1.0$ (in steps of ~0.026), and interpolated this two-dimensional grid with a cubic spline. Our interpolated grid of values is accurate to within 0.1%. For a given $N_{\rm eff}$ and $\Omega_{\rm B,0} h^2$, the final distribution of D/H values is Gaussian in shape, and offers an uncertainty on $({\rm D/H})_{\rm P}$ of $\lesssim 1\%$ over the full parameter grid; for the Standard Model, the uncertainty of the primordial deuterium abundance is ~0.83% when using the theoretical $d(p, \gamma)^3$He reaction rate. For convenience, we also provide the following simple fitting formula that describes how the D/H abundance depends on η_{10} and $N_{\rm eff}$:

$$10^5 \, ({\rm D/H})_{\rm P} = 2.47 \, (1 \pm 0.01) \, (6/\eta_{\rm D})^{1.68}, \qquad (8)$$

where

$$\eta_{\rm D} = \eta_{10} - 1.08 \, (S - 1) \, (1.1 \, \eta_{10} - 1), \qquad (9)$$

$$S = \left(1 + \frac{7\Delta N_\nu}{43}\right)^{1/2}, \qquad (10)$$

and $N_{\rm eff} = 3.046 \, (1 + \Delta N_\nu/3)$. This functional form is a slightly modified version of the form introduced by Kneller & Steigman (2004), and is accurate to within 0.4% over the range $2.3 \leqslant N_{\rm eff} \leqslant 3.7$ and $5.4 \leqslant \eta_{10} \leqslant 6.6$. The uncertainty quoted in Equation (8) includes both the 0.4% uncertainty in the form of the fitting function as well as the uncertainty in the BBN calculation.

To convert the baryon-to-photon ratio into a measurement of the cosmic density of baryons, we use the conversion $\eta_{10} = (273.78 \pm 0.18) \times \Omega_{\rm B,0} h^2$ (Steigman 2006), which assumes a primordial helium mass fraction $Y_{\rm P} = 0.2471 \pm 0.0005$ (see Equations (43)–(44) from Lopez & Turner 1999) and a present day CMB photon temperature $T_{\gamma,0} = 2.72548 \pm 0.00057$ (Fixsen 2009). Using the weighted mean value of the primordial deuterium abundance, shown in Equation (6), we estimate the cosmic density of baryons for the Standard Model:

$$100 \, \Omega_{\rm B,0} \, h^2 \, ({\rm BBN}) = 2.156 \pm 0.017 \pm 0.011, \qquad (11)$$

where the first error term includes the uncertainty in the measurement and analysis, and the second error term provides the uncertainty in the BBN calculations. This level of precision is comparable to or somewhat better than that achieved by the latest data release from the *Planck* team (Planck Collaboration et al. 2016).

The value of $\Omega_{\rm B,0} h^2 \, ({\rm BBN})$ reported in Equation (11) differs from that reported by Cooke et al. (2014) in two ways: (1) our new measure of $\Omega_{\rm B,0} h^2 \, ({\rm BBN})$ is lower by 0.00046 (i.e., a ~2.1% change); (2) the measurement uncertainty is now the dominant term of the total error budget, whereas the earlier estimate was dominated by the uncertainty in the BBN calculations. The reduced uncertainty here results from using the Marcucci et al. (2016a) $d(p, \gamma)^3$He cross-section and its estimated ~1% error. Previously, we used the Marcucci et al. (2005) calculation, which lacked a quantitative error estimate.[22] The new calculation also reduces the D yield slightly

---

[21] Our BBN model includes the effect of incomplete neutrino decoupling, which makes $N_{\rm eff} \neq 3$ at recombination for the Standard Model, as a small additive correction to the $Y_{\rm P}$ yield. BBN yields away from the Standard Model are computed by rescaling the neutrino energy density during BBN by a factor $N_\nu/3$. We then assume that the expansion rate at recombination is governed by an effective number of neutrino species, $N_{\rm eff} = 3.046 N_\nu/3$ (Mangano et al. 2005; see also, Grohs et al. 2016). To the best of our knowledge, no detailed calculation of neutrino weak decoupling has been published for expansion rates equivalent to $N_\nu \neq 3$.

[22] Our previous estimate of the $d(p, \gamma)^3$He cross-section uncertainty was based on experimental cross-section measurements below the BBN energy range (with an error of 7%). Note that both the Marcucci et al. (2005) and Marcucci et al. (2016a) calculations agree closely with these low-energy experimental data (Nollett & Holder 2011).
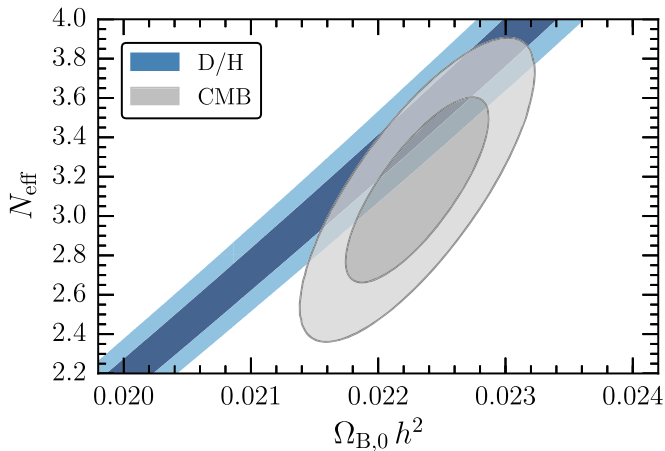
Figure 6. Comparing the expansion rate (parameterized by N_{eff}) and the cosmic density of baryons ($\Omega_{B,0}\,h^2$) from BBN (blue contours) and CMB (gray contours). The dark and light shades illustrate the 68% and 95% confidence contours, respectively.

through a combination of a better electromagnetic current operator and more careful attention to the wave function precision.[23] The Marcucci et al. (2016a) cross-section calculation results in a change to both the normalization and shape of the D/H abundance as a function of η_{10}; for the Standard Model, the primordial D/H abundance is shifted by 2.6%, and the uncertainty of this reaction rate is reduced by a factor of $\sim$4 relative to that used by Cooke et al. (2014).

The Standard Model value of the cosmic baryon density obtained from our BBN analysis is somewhat lower than that extracted from the temperature fluctuations of the CMB, $100\,\Omega_{B,0}\,h^2$(CMB) = 2.226 ± 0.023 (Planck Collaboration et al. 2016, see gray bands in Figure 5).[24] This difference corresponds to a 2.3σ discrepancy between BBN and the CMB for the Standard Model. If we consider the *Planck* fits that include high-l polarization, the significance of the disagreement becomes 2.7σ (TT,TE,EE+lowP+lensing), or 3σ in combination with external data (TT,TE,EE+lowP+lensing+ext). We also note that the central value of $\Omega_{B,0}\,h^2$ derived from the *Planck* CMB is robust; the *Planck* team consider a series of one parameter extensions to the base ΛCDM model and in all cases, the uncertainty on $\Omega_{B,0}\,h^2$ is inflated but the central value remains unchanged.

By considering a deviation in the Standard Model expansion rate of the universe, as parameterized by N_{eff}, the significance of the disagreement between CMB and BBN is reduced to the 1.5σ level.[25] This comparison is shown in Figure 6 for the *Planck* TT+lowP analysis (for similar comparisons between CMB and BBN constraints, see Cooke et al. 2014; Planck Collaboration et al. 2014, 2015; Cyburt et al. 2016; Nollett & Steigman 2015). If we assume that N_{eff} and $\Omega_{B,0}\,h^2$ do not change from BBN to recombination, then the combined confidence bounds on the baryon density and the effective

number of neutrino families are (95% confidence limits)

$$100\,\Omega_{B,0}\,h^2 = 2.235 \pm 0.071, \qquad (12)$$

$$N_{eff} = 3.44 \pm 0.45. \qquad (13)$$

The aforementioned disagreement between the CMB and BBN has emerged as a result of the improved reaction rate calculation reported recently by Marcucci et al. (2016a). To show the change introduced by this new rate, we have repeated our BBN calculations using an empirically derived $d\,(p,\,\gamma)^3$He rate, in place of the theoretical rate. We use all published data that are credible as absolute cross-sections (Griffiths et al. 1962; Ma et al. 1997; Schmid et al. 1997; Casella et al. 2002)[26] and generate Monte Carlo realizations of these experimental data, as described above. Our BBN calculations, combined with our measurement of the primordial D/H abundance is shown by Equation (6), return a Standard Model value of the cosmic baryon density:

$$100\,\Omega_{B,0}\,h^2(\text{BBN}) = 2.260 \pm 0.018 \pm 0.029, \qquad (14)$$

which is in somewhat better agreement with the Planck Collaboration et al. (2015) value, albeit with a much larger nuclear error (i.e., the second error term in Equation (14)).[27]

In the right panel of Figure 5, we compare our D/H measurements to the Standard Model deuterium abundance based on the Planck Collaboration et al. (2015) baryon density and our calculations that use the empirical $d\,(p,\,\gamma)^3$He rate. Using the empirical rate shifts the Standard Model value of the primordial D/H abundance upward by $\sim$8% and inflates the corresponding uncertainty by a factor of $\sim$1.5.

At present, it is difficult to tell how seriously to interpret the discrepancy between BBN and the CMB. Doubling the estimated nuclear error in Equation (11) still leaves us with a 2σ disagreement (assuming $N_{eff} = 3.046$). This doubling would require a $\sim$4% error on $d\,(p,\,\gamma)^3$He, which seems a large overestimate relative to the $\sim$1% errors quoted by Marcucci et al. (2016a).[28] Alternatively, the CMB and BBN would agree exactly if the Marcucci et al. (2016a) rate was scaled downwards by $\sim$10% (see, e.g., Di Valentino et al. 2014; Planck Collaboration et al. 2016); however, a significant change to the rate normalization is unlikely, given the accuracy with which rates can now be calculated for a three-body system (Kievsky et al. 2008). It is helpful that the lack of empirical information on $d\,(p,\,\gamma)^3$He at BBN energies is currently being addressed by the LUNA collaboration (Gustavino 2014). However, if they achieve high precision, their result seems unlikely to fit well with both cosmology and nuclear theory simultaneously.

6. SUMMARY AND CONCLUSIONS

Several probes of cosmology have now pinned down the content of the universe with exquisite detail. In this paper, we

---

[23] Marcucci et al. (2016a) also present BBN calculations based on their new cross-sections using the Parthenope code (Pisanti et al. 2008). At the Planck baryon density, they now find (D/H)$_P$ = 2.46×10^{-5} after a small change to their code (Marcucci 2016b). Using either the Marcucci et al. (2016a) rate or the Adelberger et al. (2011) rate for $d\,(p,\,\gamma)^3$He, there is a consistent 2% difference between their BBN code and ours.

[24] This value of $\Omega_{B,0}\,h^2$ corresponds to the TT+lowP+lensing analysis (i.e., the second data column of Table 4 from Planck Collaboration et al. 2016).

[25] The disagreement becomes more significant (2.4σ) if we consider the *Planck* TT,TE,EE+lowP analysis.

[26] Of these, only Ma et al. (1997) probe the key energy range of late-BBN deuterium burning; see Nollett & Burles (2000) and Nollett & Holder (2011) for further details.

[27] The data-driven Monte Carlo procedure that we use here has greater freedom to match S-factor data than the widely used quadratic fit of Adelberger et al. (2011), resulting in a somewhat lower $d\,(p,\,\gamma)$ rate. Adopting the Adelberger et al. (2011) S-factor curve would change Equation (14) to $100\,\Omega_{B,0}\,h^2$(BBN) = $2.225 \pm 0.018 \pm 0.033$.

[28] Similarly, other relevant reaction rates, such as $d + d$, have been measured in the laboratory with high precision and are unlikely to contribute significantly to the error budget.

build on our previous work to obtain precise measurements of the primordial deuterium abundance by presenting high-quality spectra of a DLA at $z_{abs} = 2.852054$ toward the quasar J1358+0349, taken with both the UVES and HIRES instruments. Our primary conclusions are as follows.

1. The absorption system reported here is the most metal-poor DLA currently known, with an average oxygen abundance of [O/H] = -2.804 ± 0.015. Furthermore, in one of the absorption components, we estimate [O/H] = -3.07 ± 0.03. This environment is therefore ideally suited to estimate the primordial abundance of deuterium. On the other hand, we have found an unusual amount of unrelated absorption that contaminates many of the weak, high-order D I absorption lines. Consequently, the accuracy in the determination of the D/H ratio achieved for this system is not as high as the best cases reported by Pettini & Cooke (2012a; J1419+0829) and Cooke et al. (2014; J1358+6522), see Table 3.

2. Using an identical analysis strategy to that described in Cooke et al. (2014), we measure a D/H abundance of $\log_{10} (\text{D\,I}/\text{H\,I}) = -4.582 \pm 0.012$ for this near-pristine DLA. We estimate that this abundance ratio should be adjusted by $(-4.9 \pm 1.0) \times 10^{-4}$ dex to account for D II charge transfer recombination with H I. This ionization correction is a factor of ~ 25 less than the D/H measurement precision of this system, and confirms that D I/H I $\cong$ D/H in DLAs.

3. On the basis of six high-precision and self-consistently analyzed D/H abundance measurements, we report tentative evidence for a decrease of the D/H abundance with increasing metallicity. If confirmed, this modest decrease of the D/H ratio could provide an important opportunity to study the chemical evolution of deuterium in near-pristine environments.

4. A weighted mean of these six independent D/H measures leads to our best estimate of the primordial D/H abundance, $\log_{10} (\text{D/H})_P = -4.5940 \pm 0.0056$. We combine this new determination of $(\text{D/H})_P$ with a suite of detailed Monte Carlo BBN calculations. These calculations include updates to several key nuclear cross-sections, and propagate the uncertainties of the experimental and theoretical reaction rates. We deduce a value of the cosmic baryon density $100\,\Omega_{B,0}\,h^2(\text{BBN}) = 2.156 \pm 0.017 \pm 0.011$, where the first error term represents the D/H measurement uncertainty and the second error term includes the uncertainty of the BBN calculations.

5. The above estimate of $\Omega_{B,0}\,h^2(\text{BBN})$ is comparable in precision to the recent determination of $\Omega_{B,0}\,h^2$ from the CMB temperature fluctuations recorded by the *Planck* satellite. However, using the best available BBN reaction rates, we find a 2.3σ difference between $\Omega_{B,0}\,h^2(\text{BBN})$ and $\Omega_{B,0}\,h^2(\text{CMB})$, assuming the Standard Model value for the effective number of neutrino species, $N_{eff} = 3.046$. Allowing N_{eff} to vary, the disagreement between BBN and the CMB can be reduced to the 1.5σ significance level, resulting in a bound on the effective number of neutrino families, $N_{eff} = 3.44 \pm 0.45$.

6. By replacing the theoretical $d(p, \gamma)^3\text{He}$ cross-section with the current best empirical estimate, we derive a baryon density of $100\,\Omega_{B,0}\,h^2(\text{BBN}) = 2.260 \pm 0.034$, which agrees with the *Planck* baryon density for the Standard Model. However, this agreement is partly due to

the larger error estimate for the nuclear data. Forthcoming experimental measurements of the crucial $d(p, \gamma)^3\text{He}$ reaction rate by the LUNA collaboration will provide important additional information regarding this discrepancy, since the empirical rate currently rests mainly on a single experiment, and absolute cross-sections often turn out in hindsight to have underestimated errors. The theory of few-body nuclear systems is now precise enough that a resolution in favor of the current empirical rate would present a serious problem for nuclear physics.

Our study highlights the importance of expanding the present small statistics of high-precision D/H measurements, in combination with new efforts to achieve high precision in the nuclear inputs to BBN. We believe that precise measurements of the primordial D/H abundance should be considered to be an important goal for the future generation of echelle spectrographs on large telescopes, optimized for wavelengths down to the atmospheric cutoff. This point is discussed further in the Appendix.

APPENDIX
MEASURING D/H WITH FUTURE FACILITIES

The six high-quality D/H measurements considered in this work were all observed with 8–10 m class telescopes equipped with efficient echelle spectrographs. In this Appendix, we estimate how the D/H sample size scales with telescope aperture and UV wavelength coverage. This calculation provides an indicative number of D/H systems that will be accessible to the next generation of 30–40 m class telescopes.

Starting with the Ross et al. (2013) redshift dependent quasar luminosity function, we calculate the redshift distribution of quasars brighter than those accessible with the 8–10 m class telescopes (i.e., those with apparent magnitude $m_{ref} \lesssim 19$). The magnitude limit that we have chosen corresponds to the limiting magnitude with which data of sufficient signal-to-noise ratio (i.e., S/N $\gtrsim 10$ at the bluest wavelengths) can be acquired within 1 night of 8–10 m telescope time. We integrate the quasar luminosity function over the redshift interval $z_{lim} < z < 3.5$ where $2.7 < z_{lim} < 3.5$; our chosen z_{lim} range is based on the detectability of the important, high-order weak D I lines near 915 Å. At redshifts $z_{lim} \lesssim 2.7$, the Earth's atmosphere significantly absorbs the bluest light of an

$m_{\rm ref} \simeq 19$ background quasar (i.e., at wavelengths less than $915\,\mathring{\rm A} \times (1 + 2.7) \simeq 3400\,\mathring{\rm A}$), making it impossible to reach the required S/N near the weak D I absorption lines in a reasonable amount of time. At the other limit, when $z_{\rm lim} \gtrsim 3.5$, the Lyα forest increasingly contaminates the high-order D I lines (discussed further below); note that our calculation is largely insensitive to the chosen upper limit on $z_{\rm lim}$.

The calculated redshift distribution of quasars brighter than an apparent magnitude $m_{\rm ref} = 19$ is then normalized to one. We use this normalization factor as our reference value to scale the remaining results of our calculation. This factor allows us to estimate the number of D/H measurements that can be made with future facilities for every one system that can be observed with the current 8–10 m telescopes.

We now estimate the magnitude limit of the quasars that are accessible to the three, currently planned, next generation telescope facilities: (1) The European Extremely Large Telescope (E-ELT), with a collecting area of 978 m^2, (2) The Thirty Meter Telescope (TMT), with a collecting area of 655 m^2, and (3) The Giant *Magellan* Telescope (GMT), with a collecting area of 368 m^2. Assuming all other factors to be equal, we scale the apparent magnitude limit of an 8–10 m class telescope by its collecting area:

$$m_{\rm next} = m_{\rm ref} + 2.5 \log_{10}(\mathcal{A}/\mathcal{A}_{\rm ref}), \qquad (15)$$

where $\mathcal{A}$ is the collecting area of a next generation telescope and $\mathcal{A}_{\rm ref} = 76$ m^2 is the collecting area of the Keck telescope. For the future telescopes, the typical magnitude limit is in the range $m_{\rm next} \simeq 21$–22.

This magnitude limit is comparable to the U-band brightness of a dark night sky. In order to meet our limiting magnitude criteria stated above (i.e., to acquire data of S/N $\gtrsim 10$ near the high-order D I lines), we must scale $m_{\rm next}$ (which does not include the sky background) to the limiting magnitude, $m_{\rm lim}$ (which includes the sky background). To estimate this conversion, consider the S/N equation with and without a sky background term, and demand that both cases yield the same S/N:

$$\sqrt{F_{\rm next}} = \frac{F_{\rm lim}}{\sqrt{F_{\rm lim} + F_{\rm sky}}}, \qquad (16)$$

where the desired limiting magnitude $m_{\rm lim} = m_{\rm next} - 2.5 \log_{10}(F_{\rm lim}/F_{\rm next})$, and $F_{\rm sky}$ is the sky contribution to the total flux. Solving Equation (16) for $F_{\rm lim}/F_{\rm next}$ gives

$$F_{\rm lim}/F_{\rm next} = 0.5 + 0.5\sqrt{1 + 4 \times 10^{(m_{\rm next} - m_{\rm sky})/2.5}}, \qquad (17)$$

where $m_{\rm sky} = 22.35$ arcsec^{-2} is the typical U-band brightness of a dark night sky (e.g., Patat 2008).

Assuming a Gaussian seeing profile of 0.5 arcsec FWHM, and a 0.7 arcsec entrance slit to the spectrograph, a projected slit of 1×0.7 arcsec^2 contains ~88% of the incident quasar flux; this reduction of 12% is equivalent to increasing $m_{\rm next}$ in the exponent of Equation (17) by $+0.14$ mag. Similarly, the U-band sky brightness within the projected slit is 30% lower than the value quoted above for a 1×1 arcsec^2 aperture, corresponding to a U-band sky magnitude $m_{\rm sky} = 22.74$.

The estimated limiting apparent magnitudes for the three future facilities are $m_{\rm lim}$(E-ELT, TMT, GMT) $\simeq 21.5$, 21.1, 20.6. We then integrate the Ross et al. (2013) quasar luminosity function over an apparent magnitude range brighter than the

above limits, and scale the results to the normalizing factor derived earlier for the 8–10 m class telescopes.

We now account for the *relative* Lyα forest contamination suffered by quasars over the redshift range that is considered here ($2.7 < z < 3.5$); quasars at higher redshift are more likely to have Lyα forest absorption that may contaminate the high-order D I absorption lines. To assess the relative contamination, we first need to estimate the number of pixels that are uncontaminated by Lyα forest absorption over the wavelength range of the weak D I absorption lines (≈ 915–930 $\mathring{\rm A}$ rest frame), for a DLA that has a redshift $z_{\rm abs} > z_{\rm em} - 0.2$ (where $z_{\rm em}$ is the redshift of the quasar); DLAs with a redshift close to that of the quasar are the most suitable for high-precision measures of D/H, since these DLAs will exhibit a cleaner Lyα absorption line profile, and their D I lines are less likely to be contaminated by Lyα forest absorption. We note that the condition $z_{\rm abs} > z_{\rm em} - 0.2$ is satisfied by all six high-precision measures considered in the present work (see Table 3).

We have estimated the fraction of uncontaminated pixels using the Keck Observatory Database of Ionized Absorption toward Quasars (KODIAQ) sample (O'Meara et al. 2015). The KODIAQ database consists of 170 high-quality, fully reduced, continuum normalized echelle spectra of quasars, including 93 quasars in the redshift range $2.7 < z < 3.5$. Each of these 93 quasars was visually inspected to identify the sightlines that *do not* contain a DLA with a redshift greater than $z_{\rm em} - 0.2$, since we want to estimate the severity of Lyα forest contamination in the absence of a DLA. Our final sample consists of 49 quasars, which we split into two redshift bins containing 29 quasars with $2.7 < z_{\rm em} < 3.1$ ($\langle z_{\rm em}\rangle = 2.86$) and 20 quasars with $3.1 < z_{\rm em} < 3.5$ ($\langle z_{\rm em}\rangle = 3.30$). We then calculate the fraction of pixels that exceed a normalized flux of 0.9 over the observed wavelength range $(1 + z_{\rm em} - 0.2) \times 915 < \lambda < (1 + z_{\rm em}) \times 930$, where the interval 915–930 $\mathring{\rm A}$ includes the rest-frame wavelengths of the weakest D I absorption lines. These pixels are deemed to be free of contaminating absorption. For the low-redshift subsample, we estimate a fraction of uncontaminated pixels of $\mathcal{F}(>0.9) = 0.31$; for the high-redshift subsample, $\mathcal{F}(>0.9) = 0.21$.

The number of unblended D I lines, N, is a binomially distributed random variable. To obtain a confident measure of the D I column density, we require that at least two of the five weakest D I absorption lines are unblended, yielding the probability $\Pr(N \geqslant 2) = 1 - \Pr(N = 0) - \Pr(N = 1)$. From this exercise, we estimate that $\Pr(N \geqslant 2)_{z=2.86}/ \Pr(N \geqslant 2)_{z=3.30} = 1.67$ (if we instead only require 1 D I line to be unblended, the relative probability is 1.20). Therefore, a quasar at $z = 2.86$ is roughly 67% more likely to have at least two clean D I lines, than a quasar at $z = 3.30$. To account for the increased relative Lyα forest contamination at high redshift, we scale the redshift distribution of quasars by the function

$$
\begin{aligned}
&f(z)\\
&= \left(1 + 0.67\frac{3.30 - z}{3.30 - 2.86}\right) \Big/ \left(1 + 0.67\frac{3.30 - 2.70}{3.30 - 2.86}\right),
\end{aligned}
\qquad (18)
$$

where the redshift, z, is related to the UV cutoff wavelength by the equation $\lambda_{\rm cut} = 915 \times (1 + z)$. The result of the above calculation is shown in Figure 7, where each curve illustrates the number of D/H systems that will be accessible to each facility, relative to the number that are accessible to current
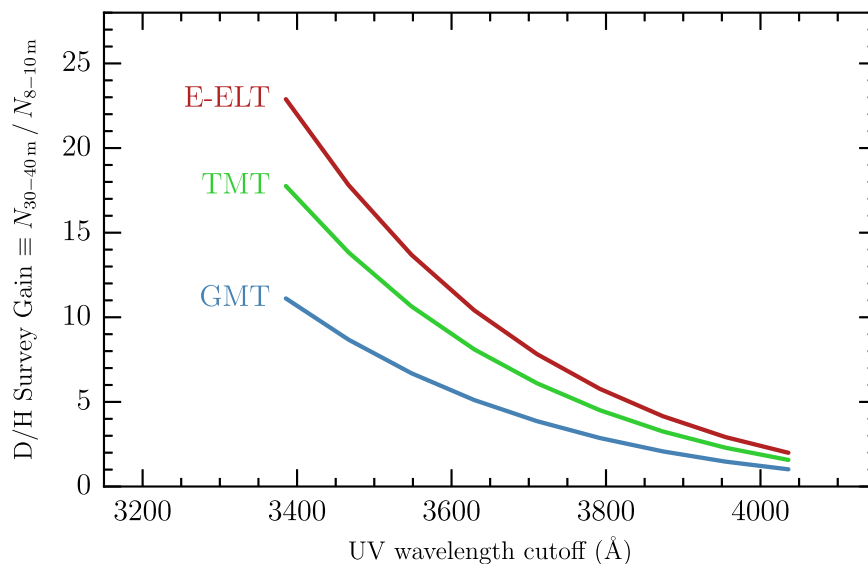
Figure 7. Each curve shows the number of D/H measurements that can be made with future telescope facilities equipped with an echelle spectrograph, relative to the number that can be made with current facilities, as a function of the "UV wavelength cutoff." The UV wavelength cutoff is defined as the observed wavelength below which the redshifted high-order D I lines (~915 Å rest frame) cannot be observed at S/N $\gtrsim$ 10 within one night of telescope time. The currently planned 30–40 m class telescopes include: (1) The European Extremely Large Telescope (E-ELT; red, curve), (2) the Thirty Meter Telescope (TMT; green curve) and (3) the Giant *Magellan* Telescope (GMT; blue curve). If the future facilities have sensitivity down to 3400 Å, the current D/H sample size will be enlarged by at least an order of magnitude.

facilities, as a function of the UV cutoff. For example, if 10 high-precision D/H measures can be made using 8–10 m telescopes, the 30–40 m class telescopes could deliver more than 200 high-precision D/H measurements, provided that the aperture gain in Equation (15) is maintained down to at least 3400 Å. Similarly, if future D/H surveys are restricted to quasars brighter than an apparent magnitude of 20.5 (equivalent to the GMT curve in Figure 7), the current statistics will be improved by over an order of magnitude.

As D/H measures are pushed toward higher precision, it will become increasingly important to observe a large sample of DLAs with diverse properties. This will allow us to better understand potentially hidden systematics, for example, due to ionization or chemical evolution. Figure 7 highlights the necessity for efficient, UV-sensitive, high-resolution spectrographs on future 30–40 m telescopes. If these capabilities can be realized, it will become possible to significantly further our measurements of D/H at high redshift, test for departures from the Standard Model, and explore the chemical evolution of galaxies via the astration of D.

REFERENCES

Adams, T. F. 1976, A&A, 50, 461
Adelberger, E. G., García, A., Hamish Robertson, R. G., et al. 2011, RvMP, 83, 195
Akerman, C. J., Ellison, S. L., Pettini, M., & Steidel, C. C. 2005, A&A, 440, 499
Aoki, W., Barklem, P. S., Beers, T. C., et al. 2009, ApJ, 698, 1803
Asplund, M., Grevesse, N., Sauval, A. J., & Scott, P. 2009, ARA&A, 47, 481
Asplund, M., Lambert, D. L., Nissen, P. E., Primas, F., & Smith, V. V. 2006, ApJ, 644, 229
Aver, E., Olive, K. A., & Skillman, E. D. 2015, JCAP, 7, 011
Balashev, S. A., Zavarygin, E. O., Ivanchik, A. V., Telikova, K. N., & Varshalovich, D. A. 2016, MNRAS, 458, 2188
Bania, T. M., Rood, R. T., & Balser, D. S. 2002, Natur, 415, 54
Bernstein, R. M., Burles, S. M., & Prochaska, J. X. 2015, PASP, 127, 911
Busemann, H., Baur, H., & Wieler, R. 2000, M&PS, 35, 949
Busemann, H., Baur, H., & Wieler, R. 2001, L&PS, 32, 1598
Casella, C., Costantini, H., Lemut, A., et al. 2002, NuPhA, 706, 203
Centurión, M., Molaro, P., Vladilo, G., et al. 2003, A&A, 403, 55
Coc, A., Petitjean, P., Uzan, J.-P., et al. 2015, PhRvD, 92, 123526
Cooke, R. 2015, ApJL, 812, L12
Cooke, R., & Pettini, M. 2016, MNRAS, 455, 1512
Cooke, R., Pettini, M., Steidel, C. C., Rudie, G. C., & Jorgenson, R. A. 2011a, MNRAS, 412, 1047
Cooke, R., Pettini, M., Steidel, C. C., Rudie, G. C., & Nissen, P. E. 2011b, MNRAS, 417, 1534
Cooke, R. J., & Madau, P. 2014, ApJ, 791, 116
Cooke, R. J., Pettini, M., & Jorgenson, R. A. 2015, ApJ, 800, 12
Cooke, R. J., Pettini, M., Jorgenson, R. A., Murphy, M. T., & Steidel, C. C. 2014, ApJ, 781, 31
Cyburt, R. H., Fields, B. D., & Olive, K. A. 2008, JCAP, 11, 012
Cyburt, R. H., Fields, B. D., Olive, K. A., & Yeh, T.-H. 2016, RvMP, 88, 015004
Dekker, H., D'Odorico, S., Kaufer, A., Delabre, B., & Kotzlowski, H. 2000, Proc. SPIE, 4008, 534
Di Valentino, E., Gustavino, C., Lesgourgues, J., et al. 2014, PhRvD, 90, 023543
Draine, B. T. 2004, in Origin and Evolution of the Elements, ed. A. McWilliams & M. Rauch, (Cambridge: Cambridge Univ. Press), 320
Draine, B. T. 2006, in ASP Conf. Ser. 348, Astrophysics in the Far Ultraviolet: Five Years of Discovery with FUSE, ed. G. Sonneborn, H. Moos, & B.-G. Andersson, (San Francisco, CA: ASP), 58
Dvorkin, I., Vangioni, E., Silk, J., Petitjean, P., & Olive, K. A. 2016, MNRAS, 458, L104
Ellison, S. L., Prochaska, J. X., & Lopez, S. 2007, MNRAS, 380, 1245
Field, G. B., & Steigman, G. 1971, ApJ, 166, 59
Fields, B. D. 2011, ARNPS, 61, 47
Fixsen, D. J. 2009, ApJ, 707, 916
Fumagalli, M., O'Meara, J. M., & Prochaska, J. X. 2011, Sci, 334, 1245
Greife, U., Gorris, F., Junker, M., Rolfs, C., & Zahnow, D. 1995, ZPhyA, 351, 107
Griffiths, G. M., Larson, E. A., & Robertson, L. P. 1962, CaJPh, 40, 402
Grohs, E., Fuller, G. M., Kishimoto, C. T., Paris, M. W., & Vlasenko, A. 2016, PhRvD, 93, 083522
Gustavino, C. 2014, in Proc. 52nd Int. Winter Meeting on Nuclear Physics, 050
Hoyle, F., & Tayler, R. J. 1964, Natur, 203, 1108
Iocco, F., Mangano, G., Miele, G., Pisanti, O., & Serpico, P. D. 2009, PhR, 472, 1
Izotov, Y. I., & Thuan, T. X. 1999, ApJ, 511, 639
Izotov, Y. I., Thuan, T. X., & Guseva, N. G. 2014, MNRAS, 445, 778
Jorgenson, R. A., Murphy, M. T., & Thompson, R. 2013, MNRAS, 435, 482

15

Jura, M. 1982, Advances in UV Astronomy: 4 Years of IUE Research, NASA CP 2238, ed. Y. Kondo, J. M. Mead, & R. D. Chapman (Greenbelt, MD: NASA), 54

Kelson, D. D. 2003, PASP, 115, 688

Kievsky, A., Rosati, S., Viviani, M., Marcucci, L. E., & Girlanda, L. 2008, JPhG, 35, 063101

Kneller, J. P., & Steigman, G. 2004, NJPh, 6, 117

Lallement, R., Hébrard, G., & Welsh, B. Y. 2008, A&A, 481, 381

Ledoux, C., Petitjean, P., Fynbo, J. P. U., Møller, P., & Srianand, R. 2006, A&A, 457, 71

Leonard, D. S., Karwowski, H. J., Brune, C. R., Fisher, B. M., & Ludwig, E. J. 2006, PhRvC, 73, 045801

Linsky, J. L., Draine, B. T., Moos, H. W., et al. 2006, ApJ, 647, 1106

Lopez, R. E., & Turner, M. S. 1999, PhRvD, 59, 103502

Ma, L., Karwowski, H. J., Brune, C. R., et al. 1997, PhRvC, 55, 588

Mangano, G., Miele, G., Pastor, S., et al. 2005, NuPhB, 729, 221

Marcucci, L. E., Mangano, G., Kievsky, A., & Viviani, M. 2016a, PhRvL, 116, 102501

Marcucci, L. E., Mangano, G., Kievsky, A., & Viviani, M. 2016b, PhRvL, 117, 049901

Marcucci, L. E., Viviani, M., Schiavilla, R., Kievsky, A., & Rosati, S. 2005, PhRvC, 72, 014001

Meléndez, J., Casagrande, L., Ramírez, I., Asplund, M., & Schuster, W. J. 2010, A&A, 515, L3

Murphy, M. T., & Bernet, M. L. 2016, MNRAS, 455, 1043

Murphy, M. T., Curran, S. J., Webb, J. K., Ménager, H., & Zych, B. J. 2007, MNRAS, 376, 673

Neeleman, M., Wolfe, A. M., Prochaska, J. X., & Rafelski, M. 2013, ApJ, 769, 54

Nollett, K. M., & Burles, S. 2000, PhRvD, 61, 123505

Nollett, K. M., & Holder, G. P. 2011, PhRvD, submitted (arXiv:1112.2683)

Nollett, K. M., & Steigman, G. 2015, PhRvD, 91, 083505

Olive, K. A., Agashe, K., Amsler, C., et al. (Particle Data Group) 2014, ChPhC, 38, 090001

O'Meara, J. M., Lehner, N., Howk, J. C., et al. 2015, AJ, 150, 111

Patat, F. 2008, A&A, 481, 575

Peebles, P. J. E. 1966, ApJ, 146, 542

Penprase, B. E., Prochaska, J. X., Sargent, W. L. W., Toro-Martinez, I., & Beeler, D. J. 2010, ApJ, 721, 1

Petitjean, P., Ledoux, C., & Srianand, R. 2008, A&A, 480, 349

Pettini, M., & Cooke, R. 2012a, MNRAS, 425, 2477

Pettini, M., & Cooke, R. 2012b, in Proc. XII Int. Symp. on Nuclei in the Cosmos (arXiv:1209.4783)

Pettini, M., King, D. L., Smith, L. J., & Hunstead, R. W. 1997, ApJ, 478, 536

Pettini, M., Zych, B. J., Steidel, C. C., & Chaffee, F. H. 2008, MNRAS, 385, 2011

Pisanti, O., Cirillo, A., Esposito, S., et al. 2008, CoPhC, 178, 956

Planck Collaboration, et al. 2014, A&A, 571, A16

Planck Collaboration, et al. 2016, A&A, 594, A13

Prochaska, J. X. 2003, ApJ, 582, 49

Prochaska, J. X., Chen, H.-W., Wolfe, A. M., Dessauges-Zavadsky, M., & Bloom, J. S. 2008, ApJ, 672, 59

Prochaska, J. X., Tripp, T. M., & Howk, J. C. 2005, ApJL, 620, L39

Prodanović, T., Steigman, G., & Fields, B. D. 2010, MNRAS, 406, 1108

Riemer-Sørensen, S., Webb, J. K., Crighton, N., et al. 2015, MNRAS, 447, 2925

Romano, D., Tosi, M., Chiappini, C., & Matteucci, F. 2006, MNRAS, 369, 295

Ross, N. P., McGreer, I. D., White, M., et al. 2013, ApJ, 773, 14

Rupak, G. 2000, NuPhA, 678, 405

Savin, D. W. 2002, ApJ, 566, 599

Sbordone, L., Bonifacio, P., Caffau, E., et al. 2010, A&A, 522, A26

Schmid, G. J., Rice, B. J., Chasteler, R. M., et al. 1997, PhRvC, 56, 2565

Spite, M., Spite, F., Caffau, E., & Bonifacio, P. 2015, A&A, 582, A74

Steigman, G. 2006, JCAP, 10, 016

Steigman, G. 2007, ARNPS, 57, 463

Steigman, G. 2012, AdHEP, 2012, 268321

Steigman, G., Werner, M. W., & Geldon, F. M. 1971, ApJ, 168, 373

Umeda, H., & Nomoto, K. 2003, Natur, 422, 871

van Zee, L., & Haynes, M. P. 2006, ApJ, 636, 214

Vladilo, G. 2004, A&A, 421, 479

Vogt, S. S., Allen, S. L., Bigelow, B. C., et al. 1994, Proc. SPIE, 2198, 362

Wagoner, R. V., Fowler, W. A., & Hoyle, F. 1967, ApJ, 148, 3

Weinberg, D. H. 2016, ApJ, submitted (arXiv:1604.07434)

Wood, B. E., Linsky, J. L., Hébrard, G., et al. 2004, ApJ, 609, 838

Zafar, T., Centurión, M., Péroux, C., et al. 2014, MNRAS, 444, 744